Research Article

Moamen S. Refat*, Ahmed Gaber, Walaa F. Alsanie, Mohamed I. Kobeasy, Rozan Zakaria, Kehkashan Alam

Utilization and simulation of innovative new binuclear Co(II), Ni(II), Cu(II), and Zn(II) diimine Schiff base complexes in sterilization and coronavirus resistance (Covid-19)

https://doi.org/10.1515/chem-2021-0068
received January 6, 2021; accepted June 14, 2021

Abstract: This article aimed at the synthesis and molecular docking assessment of new diimine Schiff base ligand, namely 2-((*E*)-(2-((*Z*)-2-(4-chlorophenyl)-2-hydroxyvinyl) hydrazono) methyl)-6-methoxyphenol (methoxy-diim), via the condensation of 1-(4-chloro-phenyl)-2-hydrazino-ethenol compound with 2-((*E*)-(2-((*Z*)-2-(4-chlorophenyl)-2-hydroxy vinyl) hydrazono)methyl)-6-methoxyphenol in acetic acid as well as the preparation of new binuclear complexes of Co(II), Ni(II), Cu(II), and Zn(II). The following synthesized complexes were prepared in a ratio of 2:1 (metal/ligand). The ^{1}H-NMR, UV-Vis, and FTIR spectroscopic data; molar conductivity measurements; and microanalytical, XRD, TGA/DTG, and biological studies were carried out to determine the molecular structure of these complexes. According to the spectroscopic analysis, the two central metal ions were coordinated with the diamine ligand via the nitrogen of the hydrazine and oxygen of the hydroxyl groups for the first metal ions and via the nitrogen of the hydrazine and oxygen of the phenol group for the second metal ions. Molecular docking for the free ligand was carried out against the breast cancer *3hb5*-oxidoreductase and the *4o1v*-protein binding kidney cancer and COVID-19 protease, and good results were obtained.

Keywords: diimine complex, thermogravimetric, COVID-19 protease, antimicrobial, molecular docking

1 Introduction

Our society is currently dealing with one of the most serious health issues, the Coronavirus. Isatin compounds were found to possess antiviral properties and were used in the treatment of HIV [1]. After virus infection, MT-4 cells infected with HIV-1 or infected human cells were incubated with various concentrations of Isatin derivatives, and the number of practical cells was determined using the 3-(4,5-dimethyl thiazol-2-yl)-2,5-diphenyltetrazolium bromide (MTT) technique [1]. In addition, the Isatin Schiff base compounds have been studied widely and were found to exhibit significant activity towards Moloney leukemia virus [2], vaccinia virus [3], rhinovirus [4], and SARS virus [5]. The mechanism of inhibition of *N*-methylisatin-*b*-40,40-diethylthiosemicarbazone (MIBDET) has been described based on the growth of the molecular leukemia virus (MLV): the MLV inhibition by M-IBDET included blocking the viral RNA translation rather than RNA interference during the viral transcription process [2]. Isatin and Isatin derivatives have also been examined for their antiviral effectiveness against acute cardiac acute respiratory syndrome [5]. The Isatin derivatives showed prohibition activity against SERS-CoV3C-like protein (3CLpro) at concentrations ranging

* **Corresponding author: Moamen S. Refat,** Department of Chemistry, Faculty of Science, Taif University, P.O. Box 11099, Taif 21944, Saudi Arabia, e-mail: msrefat@yahoo.com, moamen@tu.edu.sa
Ahmed Gaber: Department of Biology, College of Science, Taif University, P.O. Box 11099, Taif 21944, Saudi Arabia; Department of Biology, Center of Biomedical Sciences Research, Taif University, P.O. Box 11099, Taif 21944, Saudi Arabia
Walaa F. Alsanie: Department of Biology, Center of Biomedical Sciences Research, Taif University, P.O. Box 11099, Taif 21944, Saudi Arabia; Department of Clinical Laboratory Sciences, College of Applied Medical Sciences, P.O. Box 11099, Taif 21944, Saudi Arabia
Mohamed I. Kobeasy: Department of Chemistry, Faculty of Science, Taif University, P.O. Box 11099, Taif 21944, Saudi Arabia
Rozan Zakaria: Department of Chemistry, Faculty of Science, Port Said University, Port Said 42511, Egypt
Kehkashan Alam: Department of Chemistry, Faculty of Science, Aligarh Muslim University, Aligarh 202002, India

from 0.95 to 17.50 mM. The prohibited properties were tested using the fluorescence resonance energy transfer method and confirmed by HPLC analysis. Isatin-thiosemicarbazone as a preventive compound has a substantial bioactive role against a variety of viral infections [6]. Numerous compounds of 5-fluoroisatin and its derivatives were synthesized, and they displayed a significant inhibition behaviour towards different viruses and inhibited the replication process of the vesicular stomatitis virus in Vero cell lines [7].

The biological activities of Schiff bases of oximes such as hydrazone, semicarbazones, and thiosemicarbazones have been previously described [8]. Only a few variants of these chemicals showed considerable antiviral activity. For example, the 5-acyl-3-methylsulfamyl-1,2,4-triazine molecule and its derivatives were found to have antiviral activity against the coxsackie virus B4 in Vero and HeLa cell cultures, with EC50 values of 20 and 45 mg/mL, respectively [8]. The Schiff base silver(I) complexes with glycine salicylaldehyde showed good antiviral activities against the Cucumber mosaic virus [9–12]. Additionally, nickel(II), platinum(II), and palladium(II) derivatives, especially with semicarbazone and thiosemicarbazone of *p*-tolualdehyde, have been documented to show antifungal activities *in vitro* against several types of fungi such as *Alternaria alternata*, *Aspergillus niger*, and *Fusarium udum* [10–13]. In comparison to the parent ligands, the metal chelates show an excessive antifungal activity, as determined by examining these derivatives for preventing the growth of fungus. This result is attributed to the improved delocalization of the p-electrons caused by chelation, which increased the diffusion and the entry of the metal complexes to the lipid membrane, where the metal derivatives then blocked the enzymes in the microorganisms' membranes. Salicylaldehyde and 1-amino-3-hydroxyguanidine were used to determine the Schiff base. Wang et al. [14] used hydroxyaminoguanidines to modify a few basic structures of Schiff bases, resulting in the formation of unused substituted salicylaldehyde Schiff base compounds. For the first time, all of these compounds were tested against coronavirus infection and mouse hepatitis virus [14].

At this point, [1-[(30 allyl-20-hydroxy benzylidene) amino]-3-hydroxyguanidine] is the most active compound in the development of mouse hepatitis virus, roughly 376 times more active than hydroxylguanidine and around 564 times more active than hydroxyaminoguanidines. Schiff bases are versatile carbon-based molecules that are widely used and produced via the condensation reaction between various amines and aldehydes or ketones, which is known as imine. It has a wide range of applications, including pharmaceuticals, medicine, and natural activities, among others. It was also used as an oxygen sensor [15–17]. Recently, many research articles focused on the Schiff base of thiosemicarbazide and metal derivatives because of its numerous applications in the pharmacology field as antiviral, antiparasitic, antimicrobial, anticancer, and anti-HIV [15–17]. We have, therefore, undertaken the synthesis, characterization, structural, thermogravimetric, and antimicrobial studies of a few binuclear complexes formed from Co(II), Ni(II), Cu(II), and Zn(II) containing tetradentate 2-((*E*)-(2-((*Z*)-2-(4-chlorophenyl)-2-hydroxyvinyl)hydrazono) methyl)-6-methoxyphenol (methoxy-diim) Schiff base ligand.

2 Materials and methods

2.1 Synthesis of the methoxy-diim ligand

In this article, the chemicals were tested before use to emphasize their purity and their analytical structure. The ligand 2-((*E*)-(2-((*Z*)-2-(4-chlorophenyl)-2-hydroxyvinyl)hydrazono) methyl)-6-methoxyphenol (**3**) was synthesized via two steps. The first step was the reaction of *p*-chlorophenacyl bromide (**1**) with hydrazine hydrate in ethanol to give 1-(4-chloro-phenyl)-2-hydrazinoethenol (**2**). The second step was the condensation of the hydrazine derivative (**2**) with 2-hydroxy-3-methoxybenzaldehyde in acetic acid under reflux to obtain the diimine ligand (**3**, Scheme 1).

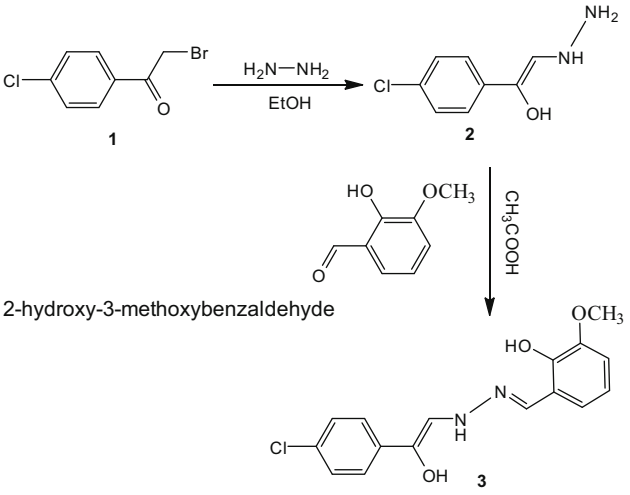

Scheme 1: Synthesis of methoxy-diim ligand (**3**).

2.2 Compound (2)

An equimolar solution of *p*-chlorophenacyl bromide (0.01 M) and hydrazine hydrate (0.01 M) was prepared in 50 mL of ethanol; then the mixture was refluxed for 2 h with heating at 70°C. After cooling the mixture, dilute acetic acid was added to neutralize it. The resulting compound was filtered, washed with water, and then recrystallized in ethanol to obtain compound (**2**). The melting point was 98°C; IR (KBr) cm^{-1} = 3,350 (br-OH), 3,320, 3,117 (NH_2), 3,230 (NH), 1,615, 1,605, 1,550 (C=C), and 1,017 (C–O); ^{1}H-NMR (DMSO-d_6) δ: 3.21 (d, 2H, NH_2), 4.20 (q, 1H, NH), 7.28–7.44 (m, 2H, Ar-H), 7.31(d, 1H, CH), and 14.07 (s, 1H, OH) ppm.

2.3 Compound (3)

A solution was prepared in 30 mL of acetic acid from the mixture of hydrazine derivative (**2**) (0.01 M) and 2-hydroxy-3-methoxybenzaldehyde (0.01 M). Then, the solution was heated under reflux for 2 h, cooled, and added into water. The resulting compound was separated out and recrystallized to give (**3**). M.P. = 140°C; IR (KBr) cm^{-1} 3,449 (br-OH), 3,046 (NH), 1,622 (C=N), 1,575, 1,486 (C=C), 1,390, and 1,271 (C–O). ^{1}H-NMR (DMSO-d_6) δ: 6.99 (s, 1H, CH=N), 7.38–7.65 (m, 8H, 2Ar-H), 9.01 (s, 1H, OH), 3.83 (s, 3H, OCH_3), and 11.16 (s, 1H, NH) ppm.

The suggested structural formula for the ligand (methoxy-diim) (Figure 1) was confirmed by the mass spectrum. The following molecular ion peaks were recorded (m/z^+): 318, 283.40, 227.86, 188.11, 135.21, 97.51, and 46.38, which correspond to $[C_{16}H_{15}N_2O_3Cl]^+$, $[C_{16}H_{16}N_2O_3]^+$, $[C_{14}H_{16}N_2O]^+$, $[C_{11}H_{12}N_2O]^+$, $[C_8H_9NO]^+$, $[C_6H_{11}N]^+$, and $[C_2H_7N]^+$ ions, respectively, that confirm the proposed molecular structure and formula.

2.4 Synthesis of solid Co(II), Ni(II), Cu(II), and Zn(II) methoxy-diim complexes

A hot solution of 1 mmol methoxy-diim ligand was prepared in 30 mL of ethanol to which a few drops of concentrated NH_4OH were added. Then, 2 mmol solutions of the following metal(II) salts, $CoCl_2{\cdot}6H_2O$, $NiCl_2{\cdot}6H_2O$, $CuCl_2{\cdot}2H_2O$, and $ZnCl_2$, were prepared in 20 mL of ethanol. Then, each metal solution was added gradually to the above solution of the methoxy-diim ligand. Ammonia solution was used to neutralize the formed mixtures (pH = 8–9), refluxed, stirred well for 2 h at 75°C, and evaporated to half its initial volume. The resulting complex was allowed to cool for a day, separated and washed with a mixture of methanol and diethyl ether. Then it was recrystallized in methanol and dried using anhydrous $CaCl_2$. Thin layer chromatography was performed to confirm its purity.

2.5 Instruments

A Jenway 4010 conductivity meter was used to measure the conductance of complex solutions (10^{-3} mol/cm^3 in DMF). The ratio of metal in the synthesized metal complexes was determined using the gravimetric method by

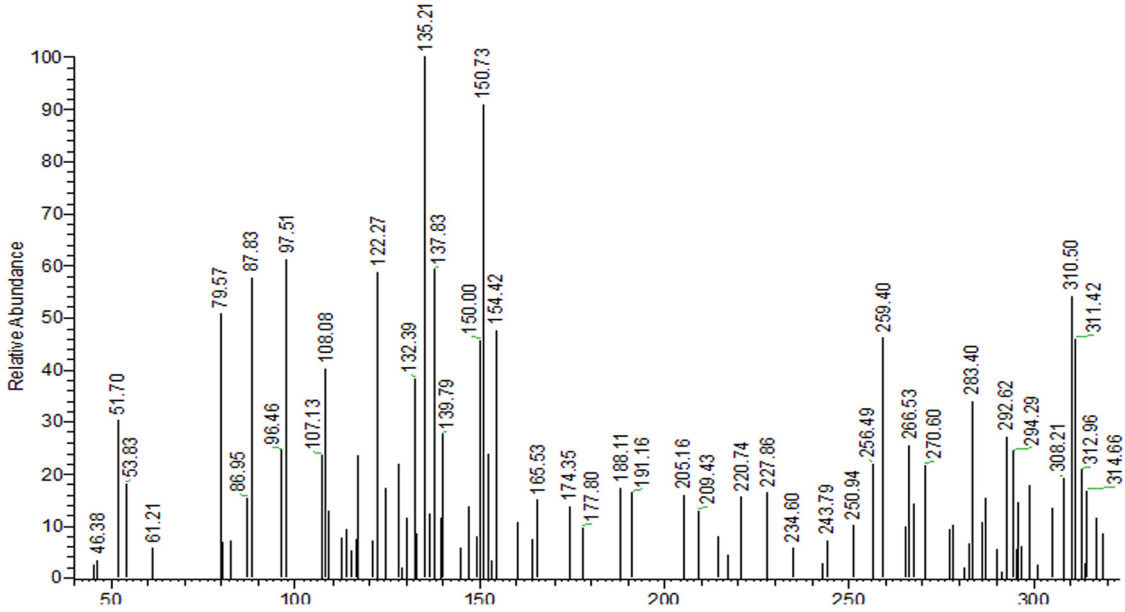

Figure 1: Mass spectrum fragmentations of the methoxy-diim ligand.

Table 1: Physicochemical studies for methoxy-diim free ligand and its metal complexes

Compounds	Colour	%Found (% Calcd)				
		C%	H%	N%	Cl%	M%
diim	Yellow	60.1 (60.28)	4.43 (4.7)	9.56 (15.07)	11.83 (11.97)	—
I	Light brown	30.2 (31.40)	4.23 (5.07)	13.52 (13.74)	17.88 (18.98)	18.97 (19.279)
II	Greenish brown	27.546 (28.96)	5.12 (5.883)	16.78 (16.896)	16.45 (16.49)	16.9 (17.708)
III	Dark green	29.5 (30.84)	3.2 (4.66)	8.5 (8.99)	17.56 (17.69)	20.05 (20.41)
IV	Dark brown	32.67 (33.55)	3.89 (4.019)	9.74 (9.786)	18.05 (18.73)	22.42 (22.85)

oxidizing it to its most stable form as well as chloride ions. The results confirmed the proposed theoretical structure for the complexes. A magnetic balance (Sherwood Scientific Cambridge, England)was used for magnetic measurements. A Bruker FT-IR spectrophotometer was used to record the infrared spectra in the range of 4,000–400 cm^{-1}; the electronic, ^{1}H-NMR (400 MHz), and thermal studies were carried out at the Cairo University. The elemental analyses (e.g. carbon, hydrogen and nitrogen) were carried out using an elemental analyser (Vario EL III Germany) at the Microanalytical Center, Cairo University. The X-ray diffraction patterns were obtained using a Bruker AXS configuration X-ray powder diffractometer.

2.6 Molecular docking

Autodock software has been utilized for the docking study. The structure of the COVID-19 protease (6LU7) was obtained from the Protein Data Bank (http://www.rcsb.org) [18]. All of the ligands were optimized using Avogadro version 1.2. In the AutoDock Tools, we have added Kollman charges and polar hydrogen atoms to the proteins, and then the grid box was chosen for the active site of the protein for ligand interactions. The results obtained from docking were visualized through Discovery Studio [18].

Ethical approval: The study was conducted and approved by the Ethical Committee approval of Taif University (1-441-26).

3 Results and discussion

3.1 Elemental analyses and physical properties

The complexes of Co(II), Ni(II), Cu(II), and Zn(II) with the 2-((*E*)-(2-((*Z*)-2-(4-chlorophenyl)-2-hydroxyvinyl) hydrazono)methyl)-6-methoxyphenol (methoxy-diim) ligand have been characterized after its synthesis. The prepared metal complexes are not reactive with atmospheric components, are non-hygroscopic and dissolve only in DMSO and DMF. The conductivities of the complexes, determined with the DMSO solution, were found

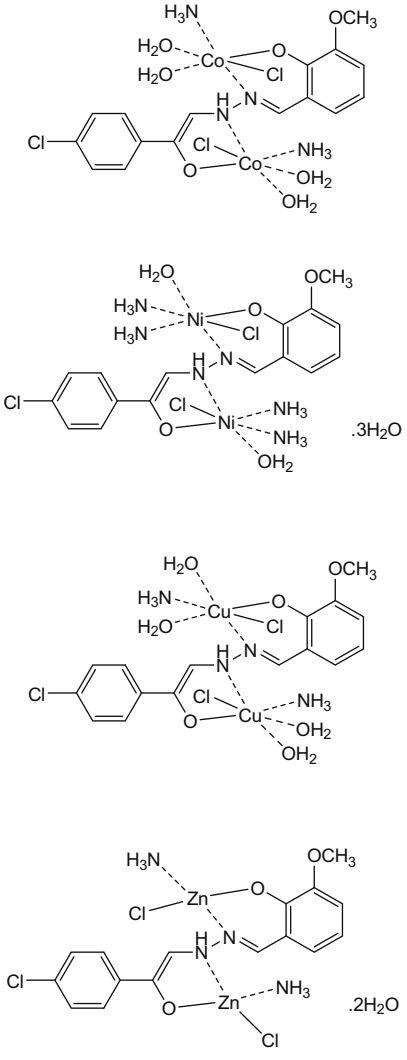

Figure 2: Proposed structures of 2:1 methoxy-diim complexes.

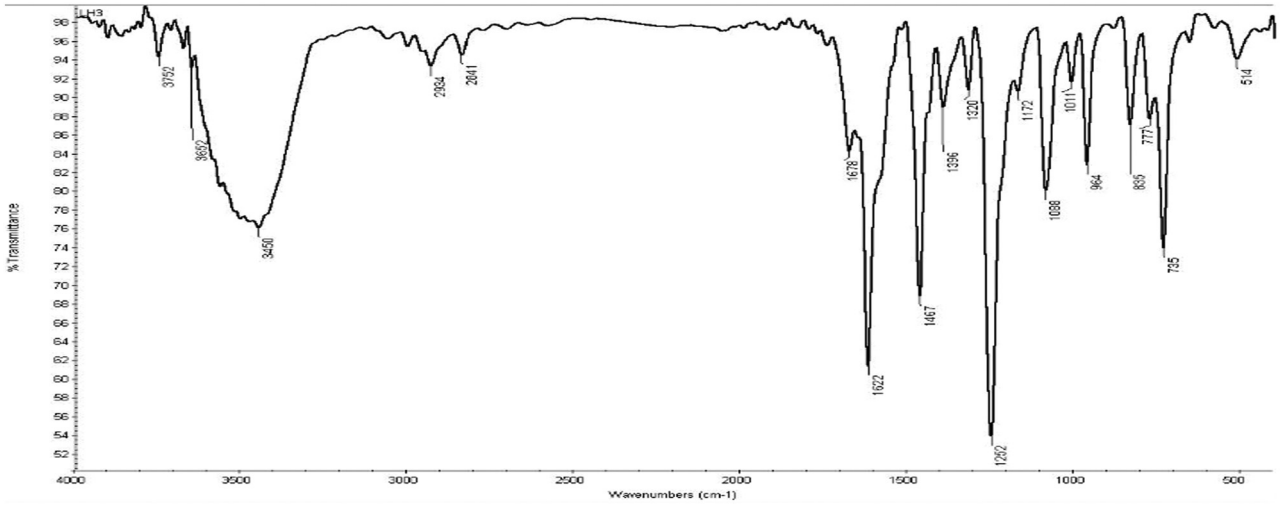

Figure 3: Infrared spectrum of the methoxy-diim free ligand.

to be lower than that of the free methoxy-diim ligand (17.83 μS), except for the Co(II) complex [18]. The results of the elemental analysis are given in Table 1. The synthesized coloured solid complexes have formulae $[Co_2(diim)(H_2O)_4(NH_3)_2(Cl)_2]$ (**I**), $[Ni_2(diim)(NH_3)_6(Cl)_2]\cdot 3H_2O$ (**ii**), $[Cu_2(diim)(H_2O)_4(NH_3)_2(Cl)_2]$ (**III**), and $[Zn_2(diim)(NH_3)_2(Cl)_2]\cdot H_2O$ (**IV**) (Figure 2).

3.2 Infrared spectral studies

The infrared spectrum of the methoxy-diim free ligand (Figure 3) was recorded, and it was noted that there are a number of distinguished vibration bands attributable to the functional groups of phenolic (Ar-OH), ketone (C═O), azomethine (C═N), phenolic (C–O), and carbon halogen bond (C–Cl) at frequencies 3,448, 3,065, 1,680, 1,622 (1,397 and 1,253), and 964 cm^{-1}, respectively, which are the essential vibration bands of the methoxy-diim ligand (Figure 3).

The corresponding spectra of Co(II), Ni(II), Cu(II), and Zn(II) complexes with the methoxy-diim ligand are shown and summarized in Figure 4 in Table 2. The medium-strong peak (1,680 cm^{-1}) of the carbonyl group found in the free methoxy-diim ligand disappeared after complexation. This result can be due to the tautomerism

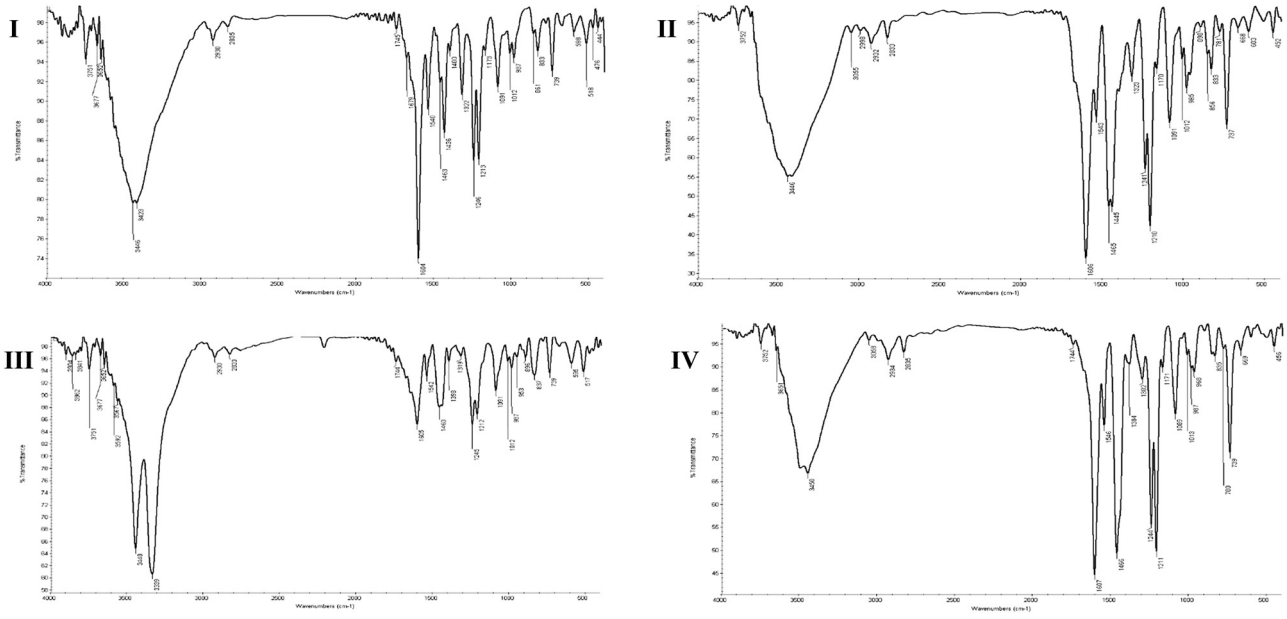

Figure 4: Infrared spectra of I: Co(II), II: Ni(II), III: Cu(III), and IV: Zn(II) methoxy-diim complexes.

Table 2: Data for infrared spectral bands (cm^{-1}) for the methoxy-diim ligand and its metal complexes

Compounds	ν(O–H)	ν(N–H)	$\nu(COCH_3)$	ν(C=O)	ν(C=N)	ν(C–O)	ν(M–O)	ν(M–N)
Methoxy-diim	3,448	3,065	2,842	1,680	1,622	1,397, 1,253	—	—
I	3,422	3,022	2,833	—	1,603	1,321, 1,213	599, 519	474
II	3,446	3,055	2,834	—	1,606	1,323, 1,210	603, 520	452
III	3,449	3,023	2,845	—	1,604	1,323, 1,091	596, 516	481
IV	3,450	3,059	2,835	—	1,607	1,302, 1,090	615	456

change in the methoxy-diim ligand from the keto to the enol form in alkaline media through the chelation process (Figure 5). In the case of the free diim ligand, the very strong peak at 1,622 cm^{-1} is due to the C=N stretching frequency of the azomethine group [19]. This stretching absorption band is withdrawn to a lower frequency range of 1,603–1,607 cm^{-1} in the prepared metal complexes, probably suggesting the coordination of the azomethine C=N group by the lone pair of electrons on its nitrogen towards the centre metal ions. The peak of the phenolic –OH group is slightly shifted to higher average frequencies than those in the spectrum of the diim ligand (3,448 cm^{-1}) because of the hydrogen bond formed among the oxygen atoms of the phenolic and nitrogen of azomethine groups (Figure 5). In the spectra of the synthesized complexes (Figure 4 **I**–**IV**), the broad bands in the frequency range 3,422–3,450 cm^{-1} are assigned to the presence of coordinated and uncoordinated water molecules [19]. From the spectrum of the free ligand and its metal complexes, the wavenumber of $\nu(COCH_3)$ (2,842 cm^{-1}) is slightly [19] changed, indicating that the $COCH_3$ group does not take part in the complexation with the metal ion. The average weak absorption peaks found in the range 855–735 cm^{-1} refer to bending vibrations $\delta(H_2O)$, emphasizing the presence of coordinated water. From the spectra of the methoxy-diim ligand, the peaks found at 1,397 and 1,253 cm^{-1} refer to the ν(C–O) stretching vibrations of the phenolic group. In the case of the vibration spectra of metal complexes, these bands are offsite to lower frequencies (1,302–1,321 and 1,090–1,213 cm^{-1}) because of the participation of the phenolic oxygen in the coordination with the metal ions. In the case of the spectra of the methoxy-diim complexes, there are new peaks in the range of 3,022–3,065 cm^{-1}, assigned to υ(NH) of the $-NH_3$ group, confirming the participation of the $-NH_3$ group and the lone pair of electrons on its nitrogen atom in the coordination reaction. In the spectra of the metal complexes, the average vibration peaks are found in the ranges of 615–516 cm^{-1} and 481–452 cm^{-1}, assigned to the vibrational motions of ν (M–O) and ν(M–N) bands, confirming the participation of oxygen and nitrogen atoms of the phenolic, hydroxyl, azomethine, and hydrazino groups in the coordination reaction with the metal [19].

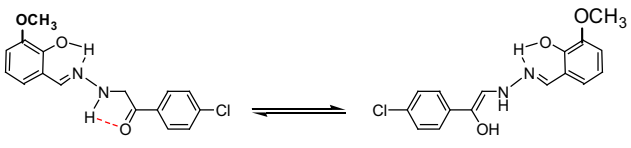

Figure 5: Tautomerism change in the methoxy-diim ligand from the keto to the enol form in the alkaline media.

3.3 Electronic and magnetic studies

In the wavelength range of 300–800 nm, the electronic absorption spectra of the methoxy-diim free ligand and its metal complexes were recorded in DMSO as a solvent. The electronic spectra of the free methoxy-diim ligand showed two peaks at 315 and 355 nm, referring to π–π* and n–π* electronic transitions [20–22]. The Co(II) complex showed three main bands at 300, 355, and 448 nm in its UV-Vis absorption spectrum: the first absorption peak was due to the intra-ligand transition of the organic moiety, and both the second and third electronic transitions were due to $^4T_{1g} \rightarrow {}^4T_{1g}(P)$ and $^4T_{1g}$ (F) $\rightarrow {}^4T_{2g}(F)$, respectively [23,24]. The octahedral geometry of the Co(II) complex was confirmed from the UV-Vis spectrum and the recorded value of its magnetic moment (5.10 B.M.) [21]. The electronic spectrum of the Ni(II) complex was found to have four electronic transition peaks at 300, 320, 360 and 400 nm. The first and second peaks may be assigned to the ligand-to-metal charge-transfer transitions, while the next two transition bands were assigned to d–d transitions of $^3A_{2g}$ (F) $\rightarrow {}^3T_{1g}$ (P) and $^3A_{2g} \rightarrow {}^3T_{1g}$ (F), respectively. The magnetic moment value of the Ni(II) complex was recorded at 2.74 B.M. From these results, the octahedral geometry was confirmed for this complex [21,22]. The electronic UV-spectrum of the copper(II) complex displayed four electronic peaks at 300, 350, 385, and 410 nm. The first two absorption peaks were assigned to

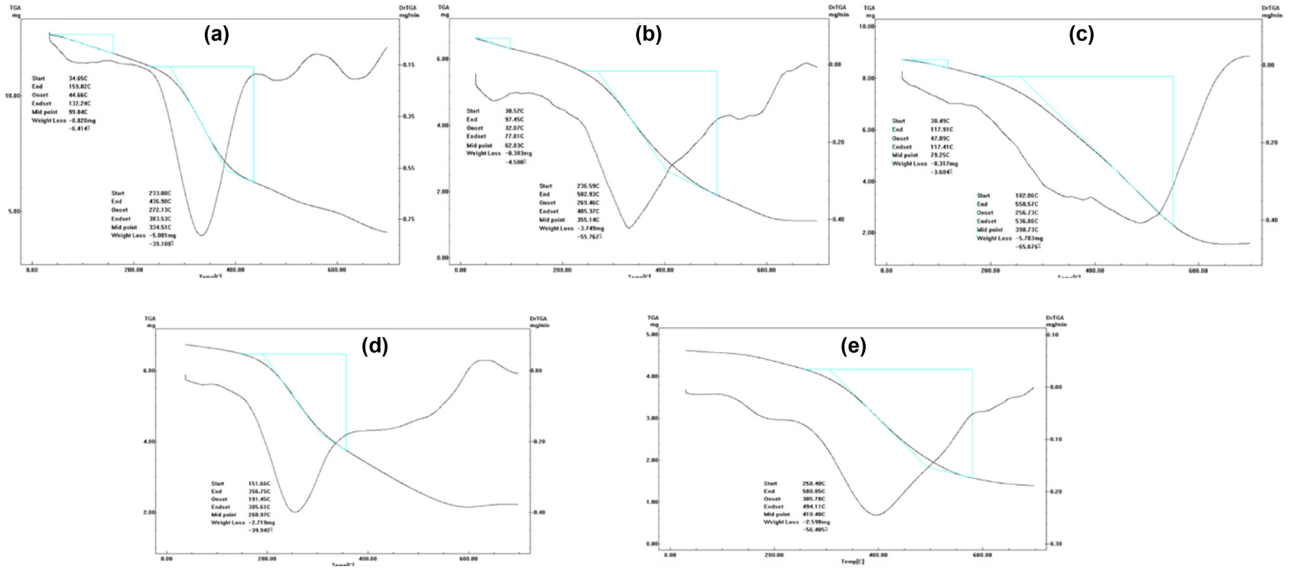

Figure 6: TGA–DrTGA curves of methoxy-diim free ligand (a), cobalt(II) complex (b), nickel(II) complex (c), copper(II) complex (d), and zinc(II) complex (e).

the ligand-to-metal charge-transfer transitions, while the second two absorption peaks, assigned to the $^2E_g \rightarrow {}^2T_{2g}$ d–d transition, were due to a distorted octahedral geometrical structure of the Cu(II) complex [21,22]. The Cu(II) complex recorded a magnetic moment of 1.66 B.M., confirming the deformed octahedral geometry [13]. The electronic spectrum of the Zn(II) complex was found to have two electronic transition peaks at 300 and 356 nm. According to the conductivity, microanalytical studies and data from the spectrum of the zinc(II) complex, its diamagnetic behaviour and tetrahedral geometry were confirmed [21,22].

3.4 ^{1}H-NMR spectral studies

^{1}H-NMR spectra for the methoxy-diim ligand and its diamagnetic Zn(II) complexes were recorded in d_6-DMSO as a solvent. The ^{1}H-NMR spectra for the investigated ligand (methoxy-diim) and its diamagnetic Zn(II) complexes were recorded in DMSO as a solvent. The chemical shift of the investigated ligand was as follows: 2.576 (d, 1H, N\\NH), 6.997 (s, 1H, CH═N), 7.381–7.423, and 7.534–7.65 for the two aromatic rings, 9.008 (s,1H, OH) ppm and 11.155 (s, 1H, OH) ppm. In the zinc complex (2:1), nearly

Table 3: Thermogravimetric data of the methoxy-diim and its metal complexes

Compounds	Steps	Temperature range/°C	DTG peak/°C	Decomposed assignments	Mass loss found (Calc.%)
diim	1st	46–205	100	diim	76.3 (76.4)
	2nd	205–536	335		
	Residue	536–700		Carbon residue	23.7 (23.6)
I	1st	35–217	57	$2H_2O + CO$	10.6 (10.4)
	2nd	217–544	330	$2NH_3 + 2N_2 + 1½Cl_2 + 7C_2H_2 + 2H_2$	63.6 (62.9)
	Residue	544–700		$2CoO$ + carbon residue	25.8 (26.7)
II	1st	40–196	114	$3H_2O$	8 (8.2)
	2nd	196–562	377	$H_2O + 2NH_3 + 3N_2 + 3H_2 + 1½Cl_2 + 8C_2H_2$	69 (69.1)
	Residue	562–700		$2NiO$	23 (22.7)
III	1st	37–180	60	$2H_2O$	5.9 (5.8)
	2nd	180–354	255	$1½Cl_2 + 5C_2H_2$	38.2 (38.2)
	3rd	354–530	423	$2H_2O + CO + 2NH_3 + H_2 + N_2$	20.6 (20.6)
	Residue	530–700		$2CuO$ + carbon residue	35.3 (35.4)
IV	1st	40–250	170	$H_2O + CO$	8.7 (8.1)
	2nd	250–580	399.6	$2NH_3 + N_2 + 1½Cl_2 + 6C_2H_2$	56.5 (57.1)
	Residue	580–700		$2ZnO$ + carbon residue	34.8 (34.8)

Table 4: Coats–Redfern (CR) and Horowitz–Metzger (HM) calculations for the methoxy-diim ligand and its metal complexes

Compound	Stage	Method	Parameter					r
			E^* (J mol^{-1})	A (s^{-1})	ΔS (J mol^{-1} K^{-1})	ΔH (J mol^{-1})	ΔG (J mol^{-1})	
diim	1st	CR	1.80×10^{-1}	7.27×10^{-9}	-4.03×10^{2}	-3.14×10^{3}	1.49×10^{5}	0.9726
		HM	4.77×10^{2}	7.78×10^{-5}	-3.26×10^{2}	-2.67×10^{3}	1.20×10^{5}	0.9692
	2nd	CR	1.56×10^{-1}	4.67×10^{-9}	-4.10×10^{2}	-5.01×10^{3}	2.42×10^{5}	0.9888
		HM	1.37×10^{3}	9.95×10^{-5}	-3.27×10^{2}	-3.64×10^{3}	1.94×10^{5}	0.9869
	3rd	CR	9.89×10^{-2}	1.44×10^{-9}	-4.23×10^{2}	-6.89×10^{3}	3.43×10^{5}	0.9518
		HM	2.10×10^{3}	8.31×10^{-5}	-3.32×10^{2}	-4.79×10^{3}	2.70×10^{5}	0.9738
I	1st	CR	5.32×10^{-2}	4.47×10^{-9}	-4.08×10^{2}	-3.48×10^{3}	1.67×10^{5}	0.9934
		HM	4.46×10^{2}	5.82×10^{-5}	-3.29×10^{2}	-3.03×10^{3}	1.34×10^{5}	0.997
	2nd	CR	1.16×10^{-1}	2.50×10^{-9}	-4.16×10^{2}	-5.18×10^{3}	2.54×10^{5}	0.9157
		HM	1.30×10^{3}	8.59×10^{-5}	-3.29×10^{2}	-3.89×10^{3}	2.01×10^{5}	0.9589
	3rd	CR	1.79×10^{-1}	5.16×10^{-9}	-4.12×10^{2}	-7.09×10^{3}	3.54×10^{5}	0.9832
		HM	2.10×10^{3}	7.75×10^{-5}	-3.32×10^{2}	-5.00×10^{3}	2.79×10^{5}	0.9913
II	1st	CR	1.02×10^{-1}	1.03×10^{-8}	-4.00×10^{2}	-3.27×10^{3}	1.54×10^{5}	0.9809
		HM	3.94×10^{2}	5.77×10^{-5}	-3.28×10^{2}	-2.87×10^{3}	1.26×10^{5}	0.9971
	2nd	CR	7.07×10^{-2}	1.34×10^{-9}	-4.22×10^{2}	-5.57×10^{3}	2.77×10^{5}	0.9694
		HM	1.56×10^{3}	9.18×10^{-5}	-3.29×10^{2}	-4.02×10^{3}	2.16×10^{5}	0.9561
III	1st	CR	1.17×10^{-1}	2.88×10^{-9}	-4.12×10^{2}	-3.98×10^{3}	1.94×10^{5}	0.9913
		HM	9.65×10^{2}	7.82×10^{-5}	-3.27×10^{2}	-3.24×10^{3}	1.54×10^{5}	0.9839
	2nd	CR	1.32×10^{-1}	3.86×10^{-9}	-4.14×10^{2}	-6.40×10^{3}	3.12×10^{5}	0.9832
		HM	2.67×10^{3}	7.77×10^{-5}	-3.31×10^{2}	-4.65×10^{3}	2.51×10^{5}	0.9788
IV	1st	CR	1.17×10^{-1}	4.50×10^{-9}	-4.08×10^{2}	-3.48×10^{3}	1.67×10^{5}	0.954
		HM	6.07×10^{2}	8.29×10^{-5}	-3.26×10^{2}	-2.87×10^{3}	1.33×10^{5}	0.916
	2nd	CR	8.31×10^{-2}	2.37×10^{-9}	-4.17×10^{2}	-5.80×10^{3}	2.85×10^{5}	0.9887
		HM	1.40×10^{3}	7.36×10^{-5}	-3.31×10^{2}	-4.40×10^{3}	2.27×10^{5}	0.9935

all of the peaks became weaker and shifted to slightly lower frequencies. The predicted structural formula of the zinc(II) complex is debated using the results from the analysis performed, confirming its tetrahedral geometry as shown in Figure 2.

3.5 Thermogravimetric studies

The TG and DrTGA thermal decomposition curves of the free methoxy-diim ligand and its metal complexes [Co(II), Ni(II), Cu(II) and Zn(II)] under a N_2 atmosphere at a heating rate of 10°C/min (Figure 6) are assigned and summarized in Table 3.

3.6 Methoxy-diim free ligand

The melting point of the diim ligand was 100°C after it underwent concurrent degradation. It was found that the ligand decomposition takes place in two main degradation steps. The first degradation phase was in the temperature range 46–205°C with equal weight loss (obs. = 10%, calc. = 11%). The second degradation phase was in the temperature range 205–536°C with equal weight loss

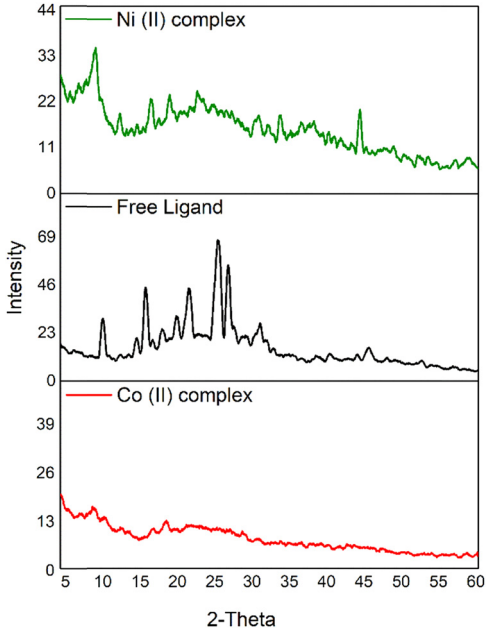

Figure 7: PXRD pattern of the free ligand, Co(II) and Ni(II) complexes.

Table 5: PXRD data of the synthesized ligand (methoxy-diim)

Pos. (°2Th.)	Height (cts)	FWHM left (°2Th.)	*d*-spacing (Å)	Rel. Int. (%)
9.6789	29.19	0.2362	9.13823	49.53
15.4503	41.87	0.2755	5.73523	71.05
17.6460	12.67	0.4723	5.02625	21.49
19.5862	16.96	0.4723	4.53251	28.77
21.3536	33.30	0.2362	4.16117	56.50
25.2967	58.94	0.2362	3.52080	100.00
26.3999	47.30	0.3542	3.37612	80.26
30.5624	10.15	0.9446	2.92513	17.22
45.3754	7.51	0.9446	1.99876	12.74
Ni(II) complex				
8.7595	16.34	0.6298	10.09524	100.00
44.1286	13.09	0.3936	2.05229	80.15

Pos. = possible; Rel. Int. = relative intensity; FWHM = full width of high maximum.

(obs. = 66.30%, calc. = 65.40%). The remaining residue until 700°C was accompanied by weight loss (obs. = 23.7%, calc. = 23.6%). All of the thermal fragments in all stages were organic moieties that were converted to gaseous phases.

3.7 Cobalt(II) complex I

From the thermal degradation curve of the Co(II) complex, it was found that it decomposes as follows: the first decomposition phase is in the temperature range 35–217°C with weight loss (obs. = 10.6 %, calc. = 10.4%), attributed to the loss of coordinated $2H_2O$ + CO. The second phase degradation takes place in the temperature range 217–544°C with a weight loss (obs. = 63.6%, calc. = 62.9%), attributed to the loss of chloride, ammonia, nitrogen, hydrogen, and acetylene gas molecules. The final residue was pure cobalt metal produced from the reduction of cobalt carbonate to cobalt(II) oxide and remained stable up to 700°C.

3.8 Nickel(II) complex II

The thermal degradation of the Ni(II) complex occurred in two main decomposition phases. The first step in the decomposition with weight loss (obs. = 8%, calc. = 8.2%) was due to the loss of three uncoordinated water molecules and two hydrogen molecules in the temperature range 40–196°C. The second degradation phase with weight loss (obs. = 69%, calc. = 69.1%) was due to the loss of chloride, ammonia, water, nitrogen gas, acetylene gas, and hydrogen gas molecules in the temperature range 196–562°C. The final residue obtained was 2NiO molecules until 700°C.

3.9 Copper(II) complex III

The thermal degradation phase of the Cu(II) complex undergoes three decomposition phases with temperature maximum values (DTG_{max}) of 60 (37–180°C), 255 (180–354°C), and 423 (354–530°C). The first phase with weight loss (obs. = 5.9%, calc. = 5.8%) was due to the loss of two water molecules with a DTG_{max} = 60°C. The phases from second to the third degradation with weight loss (obs. = 58.8%, calc. = 58.7%) due to the loss of two water molecules, ammonia gas, chloride, nitrogen, hydrogen, carbon oxide, and acetylene gas molecules with DTG_{max} values of 255 and 423°C. The final residue was CuO.

3.10 Zinc(II) complex IV

The thermal degradation of the Zn(II) complex was found to take place in two main steps with DTG_{max} = 170 (40–250°C) and 399.6 (250–580)°C. The first degradation phase with weight loss (obs. = 8.7%, calc. = 8.1%) was

Table 6: Biological evaluations for methoxy-diim ligand and its metal complexes (concentration: 10 mg/mL)

Compound	Gram-positive bacteria		Gram-negative bacteria		Fungi	
	B. subtilis	*S. aureus*	*E. coli*	*P. vulgaris*	*A. flavus*	*C. albicans*
diim	NA	NA	NA	NA	NA	NA
I	14	12	12	NA	NA	NA
II	15	18	11	NA	NA	NA
III	8	13	13	NA	NA	NA
IV	19	20	15	NA	NA	NA
Gentamycin	26	24	30	25	—	—
Ketoconazole	—	—	—	—	16	20

Table 7: Docking calculations for the methoxy-diim free ligand

Est. free energy of binding (kcal/mol)	Est. inhibition constant, K_i (μM)	vdW + Hbond + desolv energy (kcal/mol)	Electrostatic energy (kcal/mol)	Total intermolec. energy (kcal/mol)	Frequency (%)	Interact. surface
Results of diim vs 3hb5-oxidoreductase						
−6.64	13.54	−8.14	−0.13	−8.28	40	864.29
Results of diim vs 4o1v-protein						
−3.54	2.56	−5.03	−0.00	−5.03	10	628.377
Results of diim vs COVID-19 protease-protein						
−4.58	441.28	−4.68	−0.24	−4.92	50	566.515

due to the loss of water and carbon oxide with a DTG_{max} = 170°C. The second thermal decomposition with weight loss (obs. = 56.5%, calc. = 57.1%) was due to the loss of chloride, ammonia, nitrogen, and acetylene in the temperature range 250–580°C. The residual product was 2ZnO until 700°C.

3.11 Kinetic thermodynamic parameters

From the Arrhenius plots between the rate of decomposition (ln K) and $1/T$, the kinetic values such as activation energy (E^*) were computed. The Coats–Redfern and Horowitz–Metzger equations were utilized to calculate other thermodynamic parameters such as free energy ΔG^*, the enthalpy ΔH^*, and the entropy ΔS^* of the process [23,24]. Since ΔG^*, ΔH^*, and ΔS^* are relevant to the highest ratios, they are computed by the peak temperature T_s (Table 4). The prepared activated metal complexes were found to be more orderly structured than the reactants and this was proved by the negative value of ΔS^* [25] obtained.

3.12 Powder X-ray diffraction studies of the free ligand and its complexes with Co(II) and Ni(II)

The powder XRD pattern of the free ligand (diim) and complexes prepared with different ions are shown in Figure 7.

We have recorded the pattern within the range of 2θ between 5° and 60°. In the case of methoxy-diim, nine peaks have been obtained at different diffraction angles, summarized in Table 5, and therefore diim is crystalline in nature [25,26]. On the other hand, the complex of diim with Co(II) does not show any sharp peak in the XRD pattern; instead, it has noise signals that confirm its amorphous behaviour. It was noted from the data that only two peaks at diffraction angles 2θ of 8.75° and 44.12° are observed in the Ni(II) complex as shown in Table 5.

3.13 Biological assessments

The free diim ligand and its metal complexes were dissolved in DMSO to obtain a final solution with concentrations of

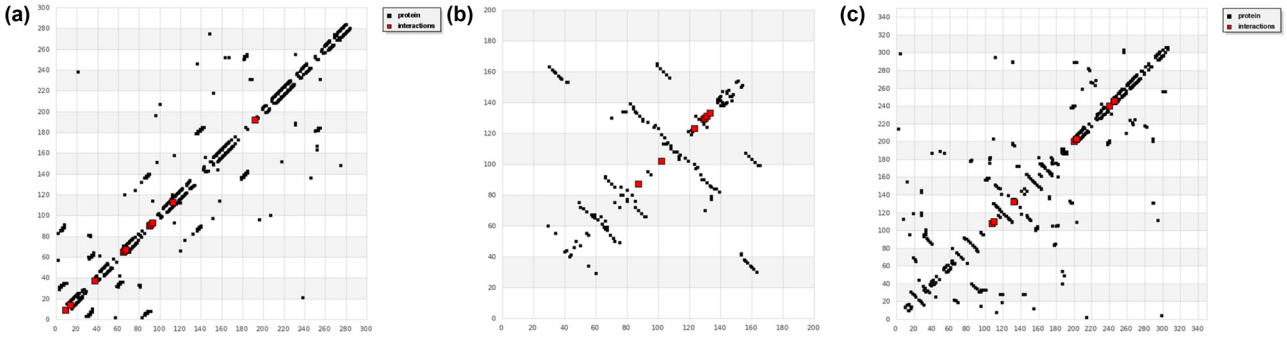

Figure 8: HB plot of the methoxy-diim ligand vs *3hb5*-oxidoreductase protein (a), 4o1v-protein binding (b), and COVID-19 protease binding protein (c).

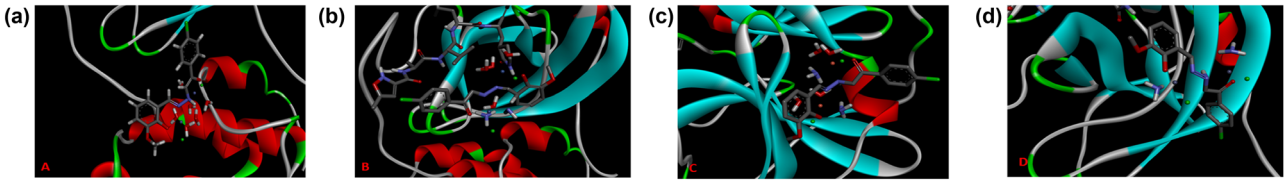

Figure 9: Docking interactions of 6LU7 with a: Co(II), b: Ni(II), c: Cu(II), and d: Zn(II) complexes.

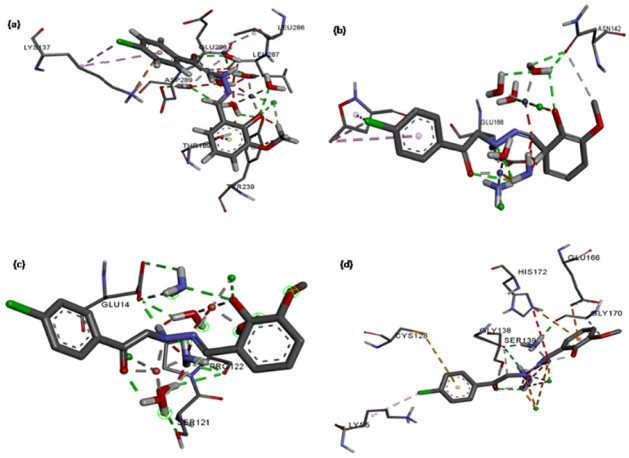

Figure 10: 3D interaction diagram showing the docking interactions of (a) Co(II), (b) Ni(II), (c) Cu(II), and (d) Zn(II) complexes with COVID-19 (6LU7).

10 and 50 mg/mL, which was used to measure the inhibition zone to determine the antibacterial activity of these compounds. As DMSO was used as a solvent it was loaded for monitoring. This activity was determined by the agar well diffusion method three times to ensure consistency of the results. *Bacillus subtilis* and *Staphylococcus aureus* were the Gram-positive bacteria used, while *Escherichia coli* and *Proteus vulgaris* were Gram-negative bacteria. From the summarized data in Table 6, we can conclude that the diim metal complexes show low average activity against *B. subtilis*, *S. aureus*, and *E. coli*. There was no activity against *P. vulgaris* for both the free diim ligand and its metal complexes. Also, they recorded no activity against *Aspergillus flavus* and *Candida albicans* species during determining their antifungal activity.

3.14 Molecular docking

The docking calculations were performed using the methoxy-diim protein model using docking server after merging the non-polar hydrogen atoms, defining rotatable bonds, adding Gasteiger charges, and other analytical parameters with the assistance of AutoDock tools [27,28]. The simulation for the docking was accomplished by Solis & Wets local search method [29,30] and Lamarckian genetic algorithm (LGA). The docking survey output results carried out for the *3hb5*-oxidoreductase (breast cancer) protein, *4o1v*-protein (kidney cancer), and COVID-19 protease binding vs the methoxy-diim free ligand are summarized in Table 7.

The methoxy-diim free ligand displayed good binding interactions with the amino acids of the protein molecules showing good stability with binding reaction energy values of −6.64, −3.54, and −4.58 kcal mol^{-1} for *3hb5*-oxidoreductase protein, *4o1v*-protein, and COVID-19 protease, respectively (Figure 8a–c).

It can be concluded that the free diim ligand can bind to the active positions in the *3hb5*-oxidoreductase protein, *4o1v*-protein, and COVID-19 protease binding protein, which means that it has a great binding affinity towards them.

The active binding site of COVID-19 was studied with the metal free ligand (diim) and all of the other complexes formed with different ions (Co, Ni, Cu, Zn). It was found from the docking study that the Ni(II) complex displays the best free energy of binding of −7.12 kcal/mol with the protease. The complex interactions of ligand and COVID-19 are shown in Figure 9.

The free energy of bindings (FEBs) with Co(II), Ni(II), Cu(II), and Zn(II) were found to be −6.19, −7.12, −6.89, and −6.79 kcal/mol, respectively. Further, the smaller binding energy shows better efficiency of binding, which is observed in the nickel complex [31], and the obtained interactions with amino acids are Glu-166 and Asn-142. So, it represents the best binding of COVID-19 protease. However, 3D interactions of Co(II), Ni(II), Cu(II), and Zn(II) complexes are shown in Figure 10 and the other docked information is summarized in Table 8.

4 Conclusion

The idea of the present research was based on preparing some of the new Schiff base compounds from the condensation reaction of the salicylaldehyde nucleus with

Table 8: Docking interaction parameters

Complexes	Binding free energy (kcal/mol)	Total intermolecular energy (kcal/mol)	Interacting amino acids
Co(II)	−6.19	−8.58	LYS137, ASP289, GLU298, LEU287, LEU 286, THR 199, TYR239
Ni(II)	−7.12	−9.21	GLU166, ASN142
Cu(II)	−6.89	−9.57	GLU14, PRO122, SER121
Zn(II)	−6.79	−8.29	GLU166, HIS172, GLY170, SER139, GLY138, LYS5, CYS128

some aromatic amines, as these types of compounds possess biological properties that are anti-bacteria, antifungal, and anti-viral. The work of this research project also extends to a theoretical and interactive simulation of the prepared compounds and their effect on the Corona virus. We were interested in preparing and characterizing four different metal Cu(II), Ni(II), Zn(II), and Co(II) complexes of the diim ligand in a ratio of 2:1 (metal/ligand). The free ligand and its metal complexes were characterized by elemental analysis, electronic analysis, FTIR, ^{1}H-NMR, XRD, and mass spectroscopy. From the FTIR spectra, it was found that the coordination process took place with the nitrogen atom of the azomethine group and the oxygen atom of the hydroxyl group for the first metal ion, while the second one formed a coordination bond with the oxygen atom of the phenol group and the other nitrogen atom of the azomethine group forming (2:1) complexes. All complexes had octahedral geometry, except for Zn(II) which had tetrahedral configuration. The thermal decomposition of both free ligand and its metal complexes occurs through two main degradation steps, with metal oxides (CoO, NiO, CuO, and ZnO) as a final residual product. The conductivity values confirmed the non-electrolytic behaviour of all of the complexes. Finally, biological evaluations were run as antibacterial, antifungal, and molecular docking. The molecular docking study reveals that the Ni(II) complex shows the best binding site with COVID-19 protease (6LU7), with a free energy of binding of −7.12 kcal/mol.

Acknowledgments: The authors are grateful to the Taif University for supplying essential facilities; they also acknowledge the support of Deanship of Scientific Research, Taif University, Saudi Arabia under project Grant No. 1-441-26.

Funding information: This work was supported by the grants from Deanship of Scientific Research, Taif University, Saudi Arabia, under project Grant No. 1-441-26.

Author contributions: Conceptualization, M.S.R. and M.I.K.; methodology, M.S.R., M.I.K. and R.Z.; software, M.S.R. and K.A.; validation, A.G., W.F.A., and M.S.R.; formal analysis, M.S.R., A.G., W.F.A., M.I.K., R.Z., and K.A.; investigation, A.G., W.F.A., and R.Z.; resources, M.S.R. and M.I.K.; data curation, M.S.R., A.G., W.F.A., M.I.K., R.Z., and K.A.; writing and original draft preparation, M.S.R., A.G., and M.I.K.; writing-review and editing, M.S.R., A.G., W.F.A., and K.A.; visualization, M.S.R. and A.G.; supervision, M.S.R.; project administration, A.G.; funding acquisition, A.G., W.F.A., and M.S.R. All authors have read and agreed to the published version of the manuscript.

Conflict of interest: All authors declare that they have no conflicts of interest.

Data availability statement: The data used to support the findings of this study are included within the article.

References

[1] Pandeya SN, Sriram D, Nath G, De Clercq E. Synthesis, antibacterial, antifungal and anti-HIV evaluation of Schiff and Mannich bases of isatin derivatives with 3-amino-2-methylmercapto quinazolin-4 (3H)-one. Indian J Pharm Sci. 1999;61:358–61.

[2] Ronen D, Sherman L, Barnun S, Teitz Y. *N*-methylisatin-beta-4′,4′-diethylthiosemicarbazone, an inhibitor of Moloney leukemia virus protein production: characterization and in vitro translation of viral mRNA. Antimicrob Agents Chemother. 1987;31:1798–802.

[3] Cooper JA, Moss B, Katz E. Inhibition of vaccinia virus late protein synthesis by isatin-β-thiosemicarbazone: Characterization and *in vitro* translation of viral mRNA. Virology. 1979;96:381–92.

[4] Webber SE, Tikhe J, Worland ST, Fuhrman SA, Hendrickson TF, Matthews DA, et al. Design, synthesis, and evaluation of nonpeptidic inhibitors of human rhinovirus 3C protease. J Med Chem. 1996;39:5072–82.

[5] Chen LR, Wang YC, Lin YW, Chou SY, Chen SF, Liu LT, et al. Synthesis and evaluation of isatin derivatives as effective SARS coronavirus 3CL protease inhibitors. Bioorg Med Chem Lett. 2005;15:3058–62.
[6] Richman DD. Antiviral drug resistance. Antivir Res. 2006;71:117–21.
[7] Abbas SY, Farag AA, Ammar YA, Atrees AA, Mohamed AF, El-Henawy AA. Synthesis, characterization, and antiviral activity of novel fluorinated isatin derivatives. Monatshefte Chem. 2013;144:1725.
[8] Mojzych M, Sebela M. Synthesis and biological activity evaluation of schiff bases of 5-acyl-1,2,4-triazine. J Chem Soc Pak. 2015;37(2):300–5.
[9] Ayşegül K-I, Demet T, EmineElçin O-E, Jan B. Novel platinum(II) and palladium(II) complexes of thiosemicarbazones derived from 5-substitutedthiophene-2-carboxaldehydes and their antiviral and cytotoxic activities. Eur J Med Chem. 2011;46(11):5616–24.
[10] Mirzabdullaev AB, Aslanova DK, Ershov FI. Prep. Induktory Interferona (Imst Biol Org Khim, Tashkent USSR). Chem Abstr. 1984;99:22191.
[11] Shelley MD, Hartley L, Groundwater PW, Fish RG. Structure-activity studies on gossypol in tumor cell lines. Anti Canccer Drugs. 2000;11(3):209–16.
[12] Meng F, Zhao Q, Li M, Xin Y. Yingyong Huaxue. Chem Abstr. 2003;138:330746.
[13] Chandra S, Tyagi M. Ni(II), Pd(II) and Pt(II) complexes with ligand containing thiosemicarbazone and semicarbazone moiety: synthesis, characterization and biological investigation. J Serb Chem Soc. 2008;73(7):727–34.
[14] Wang PH, Keck JG, Lien EJ, Lai MMC. Design, synthesis, testing, and quantitative structure-activity relationship analysis of substituted salicylaldehyde Schiff bases of 1-amino-3-hydroxyguanidine tosylate as new antiviral agents against coronavirus. J Med Chem. 1990;33(2):608–14.
[15] More MS, Joshi PG, Mishra YK, Khanna PK. Metal complexes driven from Schiff bases and semicarbazones for biomedical and allied applications: a review. Mater Today Chem. 2019;14:100195.
[16] Mondal S, Mandal SM, Ojha D, Chattopadhyay D, Sinha C. Water soluble sulfaguanidine based Schiff base as a "Turn-on" fluorescent probe for intracellular recognition of Zn2+ in living cells and exploration for biological activities. Polyhedron. 1721;2019:28–38.
[17] Roozbahani P, Salehi M, Malekshah RE, Kubicki M. Synthesis, crystal structure, electrochemical behavior and docking molecular of poly-nuclear metal complexes of Schiff base ligand derived from 2-amino benzyl alcohol. Inorg Chim Acta. 2019;4961:119022.
[18] (a) Jin Z, Du X, Xu Y, Deng Y, Liu M, Zhao Y, et al. Structure of Mpro from SARS-CoV-2 and discovery of its inhibitors. Nature. 2020;582:289–93. (b) Visualizer DS. v4.0.100. 13345. Accelrys Softw. Inc; 2005. (c) El-Habeeb AA, Refat MS. Synthesis, structure interpretation, antimicrobial and anticancer studies of tranexamic acid complexes towards Ga(III), W(VI), Y(III) and Si (IV) metal ions. J Mol Struct. 2019;1175:65–72.
[19] Nakamoto K. Infrared and Raman spectra of inorganic and coordination compounds. 4th ed. New York: Wiley; 1986.
[20] Chandra S, Gupta K. Twelve-, fourteen- and sixteen membered macrocyclic ligands and a study of the effect of ring size on ligand field strength. Transit Met Chem. 2002;27(3):329–32.
[21] Lever ABP. Crystal Field Spectra. Inorganic Electronic Spectroscopy. 1st ed. Amsterdam, The Netherlands: Academic Press; 1968.
[22] Lever ABP. Inorganic Electronic Spectroscopy. 2nd ed. Amsterdam, The Netherlands: Elsevier; 1984.
[23] Coats AW, Redfern JP. Kinetic parameters from thermogravimetric data. Nature. 1964;201:68.
[24] Horowitz HW, Metzger G. A new analysis of thermogravimetric traces. Anal Chem. 1963;35:1464.
[25] Alam K, Khan IM. Crystallographic, dynamic and Hirshfeld surface studies of charge transfer complex of imidazole as a donor with 3,5-dinitrobenzoic acid as an acceptor: Determination of various physical parameters. Org Electron Phys Mater Appl. 2018;63:7–22.
[26] Khan IM, Alam K, Alam MJ, Ahmad M. Spectrophotometric and photocatalytic studies of H-bonded charge transfer complex of oxalic acid with imidazole: single crystal XRD, experimental and DFT/TD-DFT studies. N J Chem. 2019;43:9039–51.
[27] Chourasia P, Suryesh KK, Mishra AP. Synthesis and structural investigation of some mixed-ligand selenito complexes of cobalt(II). Proc Indian Acad Sci. 1993;105:173–89.
[28] Bikadi Z, Hazai E. Application of the PM6 semi-empirical method to modeling proteins enhances docking accuracy of AutoDock. J Cheminf. 2009;1:15.
[29] Morris GM, Goodsell DS, Halliday RS, Huey R, Hart WE, Belew RK, et al. Automated docking using a Lamarckian genetic algorithm and an empirical binding free energy function. J Comput Chem. 1998;19(14):1639–62.
[30] Solis FJ, Wets RJB. Minimization by random search techniques. Math Oper Res. 1981;6(1):19–30.
[31] Shivanika C, Kumar D, Ragunathan, Tiwari P, Brindha Devi AS. Molecular docking, validation, dynamics simulations, and pharmacokinetic prediction of natural compounds against the SARS-CoV-2 main-protease. J Biomol Struct Dyn. 2020;38:1–27.